Solar Phys (2015) 290:3203–3220
DOI 10.1007/s11207-015-0649-4

A Study of the Coronal Non-thermal Velocity in Polar Regions During the Rise from Solar Minimum to Solar Maximum in Cycle 24

L. Harra[1] · D. Baker[1] · S.J. Edwards[2] · H. Hara[3] · R. Howe[4] · L. van Driel-Gesztelyi[1,5,6]

Received: 19 September 2014 / Accepted: 5 January 2015 / Published online: 23 January 2015

Abstract We explore the changes in coronal non-thermal velocity (V_{nt}) measurements at the poles from solar minimum to solar maximum using *Hinode EUV Imaging Spectrometer* data. We find that although the intensity in the corona at the poles does tend to increase with the cycle, there are no significant changes in the V_{nt} values. The locations of enhanced V_{nt} values measured do not always have a counterpart in intensity, and they are sometimes located in weak emission regions. Unipolar magnetic streams, created through diffusion of the following polarity of the decaying active regions, slowly progress towards the poles. These

Probing the Sun: Inside and Out
Guest Editors: D. Baker, L.K. Harra, and R. Howe

✉ L. Harra
l.harra@ucl.ac.uk

D. Baker
d.baker@ucl.ac.uk

S.J. Edwards
sarah.platten@dur.ac.uk

H. Hara
hirohisa.hara@nao.ac.jp

R. Howe
rhowe@nso.edu

L. van Driel-Gesztelyi
l.vandriel@ucl.ac.uk

1 UCL-Mullard Space Science Laboratory, Holmbury St Mary, Dorking, Surrey, RH5 6NT, UK

2 Department of Mathematical Sciences, South Road, Durham, UK

3 National Astronomical Observatory of Japan, Osawa, Mitaka, Tokyo 181-8588, Japan

4 School of Physics and Astronomy, University of Birmingham, Edgbaston, Birmingham B15 2TT, UK

5 Observatoire de Paris, LESIA, CNRS, UPMC Univ. Paris 06, Univ. Paris-Diderot, Meudon, France

6 Konkoly Observatory, Hungarian Academy of Sciences, Budapest, Hungary

streams are expected to be related to magnetic nulls as locations that indicate an increased likelihood for magnetic reconnection to occur. Through global potential field source-surface modelling, we determine how the number of nulls varied during the cycle and find that those that lie at < 1.1 solar radii vary significantly. We search for a correlation between the variation of the magnetic nulls and the $V_{\rm nt}$ values, as it may be expected that with an increasing number of nulls, the $V_{\rm nt}$ values in the corona increase as well. There is no correlation with the $V_{\rm nt}$ values, however. This indicates that the magnetic structures that create the enhanced $V_{\rm nt}$ behaviour are small-scale features and hence not easily measurable at the poles. Because they do not change during the solar cycle, they are likely to be created by a local dynamo. The variation of the upper range of $V_{\rm nt}$ is reduced, which highlights that strongly dynamic behaviour is reduced as the solar maximum approaches. This is likely to be due to the reduced area of the polar coronal hole, which allows fewer opportunities for reconnection to occur between open and closed magnetic fields.

Keywords Solar cycle · Coronal holes

1. Introduction

Changes in solar activity have been observed for centuries (see for example Hathaway (2010) for a review of the solar cycle). This cyclic behaviour is approximately described through Hale's polarity law, where the preceding and following sunspots are generally of opposite polarity. The corresponding spots in the northern and southern hemispheres are also of opposite sign. In addition, Joy's law describes how the following spot tends to appear farther from the equator than the preceding spot, and the higher the latitude, the greater the inclination to the axis. As the cycle begins, the higher latitude fields are transported towards the opposite polarity polar fields where flux cancellation eventually reverses the magnetic polarities of the poles. Babcock (1959) observed that the polar fields reversed approximately at solar maximum, with the timings of the reversals at the north and south poles being offset from each other. The polar fields will be at their peak at solar minimum. This behaviour is clearly seen from the well-known magnetic butterfly diagram (*e.g.* Hathaway, 2010).

The polar fields are critical for understanding the global behaviour of the Sun's magnetic field and the solar activity cycle. Photospheric fields have been measured by the Wilcox Solar Observatory (WSO) and by the National Solar Observatory instruments at Kitt Peak for several solar cycles. The WSO measurements have been used to monitor the polar fields in particular. These data clearly show the march of the field of the decaying active regions to the poles, as described by Babcock (1959), and the reversal of the polar fields. Howe *et al.* (2013) compared this poleward migration rate of the magnetic field seen in the Kitt Peak butterfly diagram and found it to be consistent with the sub-surface meridional flow. Petrie, Petrovay, and Schatten (2014) have studied observational evidence of the cyclical behaviour of active regions and polar magnetic fields through a range of observations, from below the surface. They found that their observations are consistent with the Babcock model. Recent work by Mordvinov and Yazev (2014) examined Cycles 21 – 24, and the authors found that the appearance of unipolar magnetic fields is determined by the decay of long-lived activity complexes. They comment on the non-uniformity of the sunspot distribution and the North–South asymmetry and on the impact these factors have on the polar-field reversals. The recent solar minimum and rise to maximum have been observed by the *Solar Optical Telescope* (SOT; Tsuneta *et al.*, 2008) onboard *Hinode*. This instrument allows measuring the photospheric vector magnetic field, which has been used to measure the polar fields

more accurately (but in a small field of view). Shiota *et al.* (2012) found that the detected magnetic flux values in magnetic concentrations in polar regions range over four orders of magnitude. All of the large magnetic patches ($> 10^{18}$ maxwell (Mx)) have the same magnetic polarity, while the smaller patches have a reasonable balance of both polarities. The polarity of the poles is dominated by the large magnetic flux. A decrease in the net flux is observed during the rise phase of the current cycle, with this being more rapid in the North than in the South. They found that the decrease in magnetic flux is due to a reduction in the number and size of large flux concentrations as well as to the appearances of patches of opposite polarity at lower latitudes. They also pointed out that the number and field strength of the large magnetic flux concentrations started to decrease during the extended solar minimum period, which suggests that this reduction does not entirely rely on the dispersed active region magnetic field.

Solar cycle variations of the number and complexity of active regions and the intensity of flares have been well observed over many solar cycles (Hathaway, 2010). However, weaker solar activity such as coronal bright points have been harder to measure until the launch of the *Yohkoh* spacecraft (Ogawara *et al.*, 1991) in the early 1990s. Hara and Nakakubo-Morimoto (2003) studied the number of X-ray bright points during the period between 1993 and 2000 and found that the number density of bright points in the quiet-Sun area is nearly independent of the solar cycle (as first reported by Golub *et al.* 1974), while the total number over the disk is anti-correlated with the sunspot numbers (Davis, 1983) as a result of the reduced quiet-Sun area across the disk. This is due to emergence of active regions and the change of the foreground/background coronal brightness that is correlated with the sunspot numbers. This suggests that there may be different mechanisms creating magnetic fields associated with small-scale bright points and those of large-scale active regions. A different behaviour was found for bright points in the quiet Sun and active Sun. The *Solar and Heliospheric Observatory* (SOHO) *EUV Imaging telescope* (EIT; Delaboudinière *et al.*, 1995) observed the coronal bright points for all of Cycle 23, as described by Sattarov *et al.* (2010). They also found a different behaviour for bright points in the quiet Sun and active Sun. The quiet-Sun bright points are distributed evenly across the disk and show a slight decrease at the maximum of solar activity. As discussed earlier, this is most likely related to the change in the fraction of the solar surface occupied by the quiet Sun at these times. McIntosh and Gurman (2005) reported similar results based on a study of coronal bright points over a nine-year period. Furthermore, they found that the lifetimes of the quiet-Sun bright points also do not vary with the cycle. All of these factors suggest that the process creating these bright points is cycle independent.

The cycle variation of the large-scale corona is believed to track the activity-belt behaviour. This was confirmed recently by Morgan and Habbal (2010), who highlighted the change from the solar minimum period, when streamers are more or less confined to the equatorial region, to the maximum period when streamers extend to higher latitudes and are more complex. The transition between the time when the large streamers are confined to a single plasma sheet close to the equator to when they become more complex at maximum is observed to occur very abruptly. The polar footprints of the streamers are often above polar crown filaments, while the equatorial footprints can be above filaments or active regions. Observations of the corona in the elusive region up to 2.5 solar radii ($R_\odot$) have been made by the *Sun Watcher with Active Pixels and Image Processing* (SWAP) EUV telescope onboard the PROBA-2 spacecraft. Seaton *et al.* (2013) analysed data to a height of 1.7 $R_\odot$ in the EUV over the three-year period around the rise of Solar Cycle 24. They highlighted persistent bright and diffuse features with open fields that overlie polar crown filaments and extend to large heights. The mean brightness above 1.3 $R_\odot$ in particular is related to

the sunspot activity, and they observed a difference in behaviour between the northern and southern hemispheres.

Modelling work by Pinto *et al.* (2011) coupled the solar dynamo and corona during an activity cycle and found that the polarity reversal occurs quickly in the corona even if the underlying magnetic field evolves slowly. They found that magnetic polarity reversal occurs at different rates at different coronal heights at the polar regions. The progression of the polarity reversal is fast between 2 and 15 $R_{\odot}$. From there downwards it slows considerably with a delay of six months between 2 and 1.6 $R_{\odot}$ and a further delay of one year between 1.6 and 1.3 $R_{\odot}$. Simulations have been carried out to track the changes in the large-scale magnetic field. Yeates (2014) has used coupled magnetic flux transport and magneto-frictional simulations to track the magnetic evolution for a 15-year period from 1996. He used these simulations to determine that flux ropes are more prevalent outside of active latitudes, but those at active latitudes are more frequently ejected. Platten *et al.* (2014a) have explored the magnetic topology of the solar cycle using a potential field source surface approximation. They found that at solar maximum the global coronal field involves a multitude of topological structures criss-crossing at all latitudes throughout the atmosphere. At solar minimum the coronal topology is more strongly influenced by the global dipole.

In this article, we analyse the variation of the non-thermal velocity ($V_{\rm nt}$) at the poles from the start of 2007 until 2013 with *EUV Imaging Telescope* (EIS; Culhane *et al.*, 2007) onboard *Hinode*. This covers the period of the extended solar minimum and the rise to the solar maximum in Cycle 24. Dynamical behaviour has been observed spectroscopically in polar coronal holes. This takes the form of jets and brightenings. Coronal jets have been found by Kamio *et al.* (2009) to be connected to the patches of vertical kG fields in the photosphere. Explosive events and other cool upflows are found to occur in network regions with low-lying fields. Bright points are observed in coronal holes as small loops, with many other bright points appear as point-like structures (Doschek *et al.*, 2010). During the period from 2007 to 2013, the flows of opposite polarities to the poles lead to polarity reversal, with the north pole changing polarity first. We searched for changes in the non-thermal velocity and intensity in the coronal holes when the opposite magnetic polarity streams reach the poles. We intend to determine whether the magnetic polarity streams affect the small-scale dynamics at the poles, or whether this process is too slow to change the small-scale activity levels. We compare our results with global magnetic field modelling to determine whether there are correlations with the opposite polarity streams, dynamics in the corona, and the number of magnetic nulls expected.

2. Data Analysis and Simulations

We analysed data from *Hinode* EIS. *Hinode* has been observing the north and south poles at regular intervals since its launch at the end of 2006. For each raster we followed the standard calibration procedure using the eis_prep routine in SolarSoft (Freeland and Handy, 1998). The slit tilt and orbital variation of the line position were removed. Since coronal holes are weak in coronal emission, we concentrated on the strongest emission line Fe XII at 195.12 Å ($\log T = 6.1$). Each spectrum was fitted with a single Gaussian profile, and the line intensity and width were determined. The line width measurements were converted into non-thermal velocity by removing the instrumental and thermal width. We made use of the SolarSoft routine eis_width2velocity within the EIS software tree. This uses the equation

$$\mathrm{FWHM}^2 = (\mathrm{instr}_{\mathrm{fwhm}})^2 + 4\ln(2)(\lambda/c)^2\left(v_{\mathrm{t}}^2 + (v_{\mathrm{nt}})^2\right), \tag{1}$$

where v_t is the thermal velocity, FWHM is the full width at half maximum of each line profile, λ is the wavelength of the peak of the emission line, c is the speed of light, v_{nt} is the non-thermal velocity, and instr_{fwhm} is the instrumental width. We chose to concentrate on the non-thermal velocity measurements, since there is less impact of line of sight from centre to limb than for Doppler velocity measurements. An example using the *Yohkoh Bragg Crystal Spectrometer* data by Mariska (1994) found that the line widths of solar flare spectra when measured at the centre of the solar disk are not different from those measured at the limb. The Doppler velocity measurements would be dependent on the location on the disk, and hence we excluded them from this work. We processed data from both North and South polar raster scans. For each scan we focused only on data that excluded the limb and above-limb data to keep the datasets consistent. We then produced histograms of each raster and measured the peak value (called V_{nt}^{peak}) and 10 % of the maximum of the histogram (called V_{nt}^{upper}) to understand how the values are varying with time. The V_{nt}^{upper} values give an indication of high-velocity end of V_{nt} values, which are indicative of phenomena such as jets. We did not fit spectral lines when the data quality was too low.

The *Hinode X-ray telescope* (XRT; Golub *et al.*, 2007) was used for context imaging. The synoptic composite data were used, which are available at http://solar.physics.montana.edu/HINODE/XRT/SCIA/latest_month.html. The EIS data were rotated to the time of the XRT synoptic image in each case.

We analysed *Solar Dynamics Observatory* (SDO)-*Atmospheric Imaging Assembly* (AIA; Lemen *et al.*, 2012) data to determine the number of coronal bright points in the polar regions. We analysed the AIA data at the 211 Å band; they were obtained every 12 s. We chose to analyse one full month of data every three months because of the large volume of data. At each of our three-month sampling interval, the 211 Å data were sampled every five minutes for the period of a month to examine the long-term variation of coronal bright points over the Sun. The basic method for identifying the bright points is the same as that used by Hara and Nakakubo-Morimoto (2003), but we reduced the image size from the original 4096 × 4096 pixels to 1024 × 1024 pixels by 4 × 4 pixel summation to enhance the detection efficiency for a deep survey and to shorten the processing time. The number of coronal bright points above a high latitude, 50° in this article, has a large seasonal variation due to the change of the corresponding area caused by the tilt of the rotation axis relative to the observer, as we describe below (Figure 11). This was corrected for.

The butterfly diagram of net photospheric magnetic flux was constructed using US National Solar Observatory/*Global Oscillation Network Group* (GONG) integral Carrington rotation magnetogram synoptic maps for the period 2007 – 2014 (http://gong.nso.edu/data/magmap/crmap.html). Daily observations of the magnetic field along the solar central meridian were inserted at the appropriate Carrington longitude of the GONG synoptic maps. The longitudinally averaged radial magnetic field was then used to produce the two-dimensional latitude-time diagrams.

The coronal magnetic field was extrapolated from synoptic magnetograms from the *Solar Optical Long-term Investigations of the Sun* (SOLIS; Gosain *et al.* 2013) telescope and have a resolution of 360 gridpoints equally spaced in longitude and 180 grid points equally spaced in sine latitude. We used these magnetograms as a lower boundary condition to the potential-field source-surface (PFSS) model (Schatten, Wilcox, and Ness, 1969; Altschuler and Newkirk, 1969). The extrapolated potential field has 329 grid points equally spaced in longitude, 165 gridpoints equally spaced in latitude, and 48 grid points exponentially spaced radially between $1R_\odot$ and $2.5R_\odot$.

We found the number of null points in these extrapolations using the trilinear null-finding method (Haynes and Parnell, 2007). The number of null points found in the extrapolation

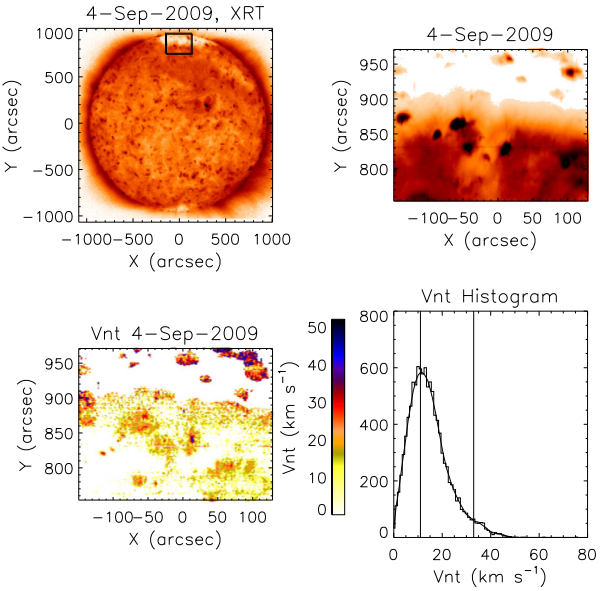

Figure 1 An example of data for the 4 September 2009 for the north pole. The top left panel shows the XRT image with the EIS field of view shown as a black box. The top right image shows the EIS intensity image. The intensity is shown in reverse colour, which means that dark is the highest intensity and light is the weakest. The bottom left panel shows the non-thermal velocity derived from the Fe XII emission line, the bottom right panel shows the histogram of the non-thermal velocity.

is very much dependent on the resolution of the extrapolation. Therefore, it is important to consider trends in the numbers of null points rather than the just the numbers. Since we have a resolution lower than 1°, we expect to miss many null points associated with small magnetic fragments. Near the poles we do not have good coverage in the synoptic magnetogram, and the sine latitude scaling means that we only have two grid points above 80° latitude in the original magnetograms. Therefore we did not include null points with latitudes greater than 80° when we calculated the numbers of nulls near to the poles.

3. Results

Figure 1 shows an example of the datasets that we analysed from 4 September 2009 during the period when the Sun was close to solar minimum. The image shows the intensity measured from the Fe XII emission line with the region that we focused on highlighted by a black box. The non-thermal velocity "image" shows strong regions of non-thermal velocity around the bright points, and there is a slight increase along the coronal hole boundary. When comparing the intensity and non-thermal velocity images, it is clear that there is no one-to-one correlation between these parameters. The non-thermal velocity appears higher in weak intensity regions that have strong dynamics, and vice versa. The peak of the histogram and the 10 % of the maximum value are highlighted in the plot.

Figure 2 shows diffuse coronal regions with a few bright points evident in the intensity image. The $V_{\rm nt}$ image also shows enhancements, but they are not necessarily in the same place as the strongest intensity regions. A strong $V_{\rm nt}$ region centred at $x = 0''$ and $y = 700''$ has no intensity counterpart. There is also a tendency for higher $V_{\rm nt}$ values to exist at the edge of the diffuse region, *i.e.* along open coronal hole boundaries at the interface between open and closed field. This is to be expected because the closed magnetic structures of the diffuse corona and the open magnetic structures that exist in the coronal holes probably interact. In this example the peak of $V_{\rm nt}$ is 16 km s^{-1} and $V_{\rm nt}^{\rm upper}$ is 42 km s^{-1}. $V_{\rm nt}$ scales differ from image to image.

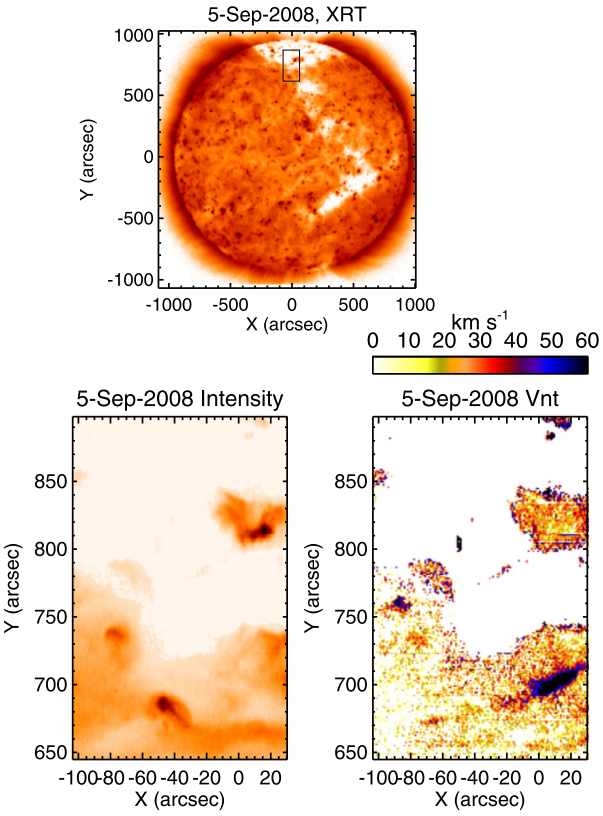

Figure 2 The top image is the XRT image with the EIS field of view shown as a black box. The intensity plot (bottom left) and non-thermal velocity (bottom right) for 5 September 2008. The weakest intensity regions have not been analysed because the data quality was too poor. The intensity is illustrated in reverse colour. Regions of high non-thermal velocity are seen within the diffuse region with the largest feature at approximately $x = 0''$ and $y = 700''$. There are also strong non-thermal velocities seen at the edges of the diffuse region and the coronal hole.

Another example, shown in Figure 3, has a lower $V_{\rm nt}$ peak value of 9 km s^{-1} and $V_{\rm nt}^{\rm upper}$ value of 33 km s^{-1}, both of which are weaker than those in Figure 2. Distinct enhancements are seen in the $V_{\rm nt}$ images that have no counterpart in the intensity image. There is an elongated $V_{\rm nt}$ feature that is centred at $x = 20''$, $y = 720''$, which is likely to be associated with a jet. There are also enhanced $V_{\rm nt}$ values at the edges of the diffuse structure.

Figure 4 shows an example later in the cycle in 2011. The $V_{\rm nt}$ peak is 13.5 km s^{-1} and $V_{\rm nt}$ upper is 24 km s^{-1}. There are no significant $V_{\rm nt}$ enhancements, but there is a scattering of stronger regions throughout the raster. Bright points are also seen in the intensity image.

Figure 5 shows two EIS rasters taken consecutively in time. A comparison of the intensity and $V_{\rm nt}$ images from the two rasters illustrates how dynamic the polar region is. Different intensity features are seen at the two different times, and strong $V_{\rm nt}$ features come and go with time. However, the histograms of $V_{\rm nt}$ at these two times show similar values. The $V_{\rm nt}^{\rm upper}$ values are 32 km s^{-1} at both times, and the $V_{\rm nt}^{\rm peak}$ values are 15 km s^{-1} for the first time and 14 km s^{-1} for the second time.

Figure 6 shows an example of the relationship between $V_{\rm nt}$ and intensity within the raster at 05:31 UT on 22 September 2009 displayed in Figure 5. There is no direct correlation, with low-intensity regions having the full range of non-thermal velocities. However, there is a trend for the highest $V_{\rm nt}$ to be seen in the lower intensity regions.

In Figure 7 the results of the histograms of $V_{\rm nt}$ for all the rasters in the north pole are plotted. The value of the peak of $V_{\rm nt}$ remains approximately unchanged from solar minimum to maximum. There is no indication of an increase during the rise to solar maximum. This

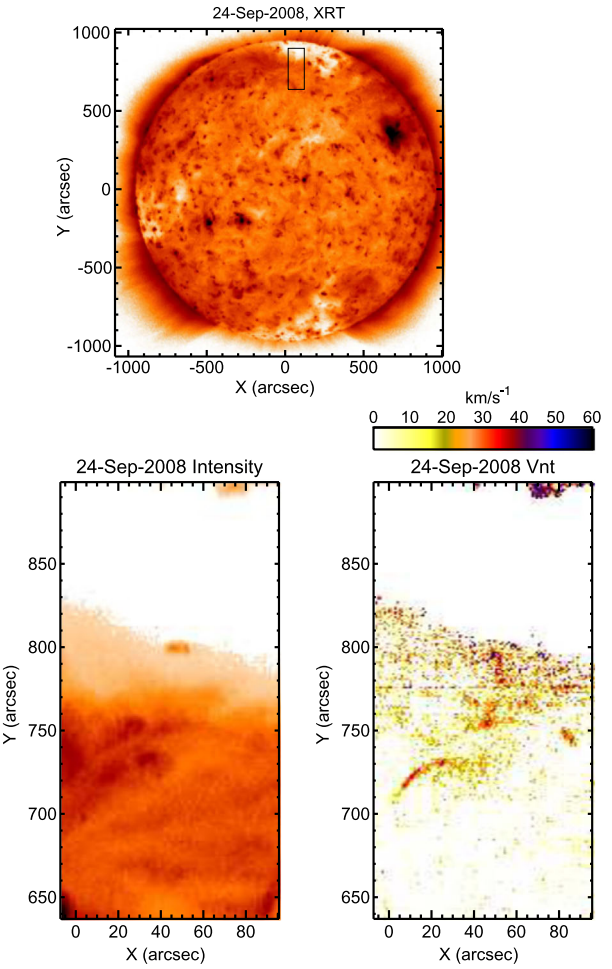

Figure 3 The top image shows the XRT image with the EIS field of view shown as a black box. The intensity plot (bottom left) and non-thermal velocity (bottom right) for 24 September 2008. The weakest intensity regions have not been analysed because the data quality was too poor. The intensity is illustrated in reverse colour. Regions of high non-thermal velocity are seen within the diffuse region with the largest feature at approximately $x = 20''$ and $y = 730''$. This feature has lower non-thermal velocity values than those seen on 5 September 2008. There are also strong non-thermal velocities seen at the edges of the diffuse region and the coronal hole.

indicates that the amount of dynamics at the poles remains at a steady level. There is no dramatic increase or decrease in the values, and the peak values of the histogram do not reach above $\approx 30\ \mathrm{km\,s^{-1}}$. The plot showing 10 % of the maximum of the histogram, ($V_{\mathrm{nt}}^{\mathrm{upper}}$) was included to determine if there was an increase in the dynamics of the plasma at any point during the change in the activity levels. There is more variation in this plot, which is to be expected, as higher non-thermal velocities will be measured during a jet, for example. As a result the rastering nature of the instrument, not all jets that occur within the field of view and time period of the raster will be seen. Although the upper range of the non-thermal velocity shows more scatter, there is no strong trend for the highest values of the non-thermal velocity reached to increase with the cycle of activity, although from 2012 onwards the lowest values are higher than those of the previous years. On the other hand, the highest values are lower than at earlier times. The spread of values has decreased but the values always fluctuate around $30\ \mathrm{km\,s^{-1}}$. The intensity, however, does start to increase in a more consistent way with time, and this seems to be due to the increasingly diffuse corona and large loops. The coronal hole is clearly visible until 2010, when more diffuse corona appears, and the intensity increase that we observe is related to this.

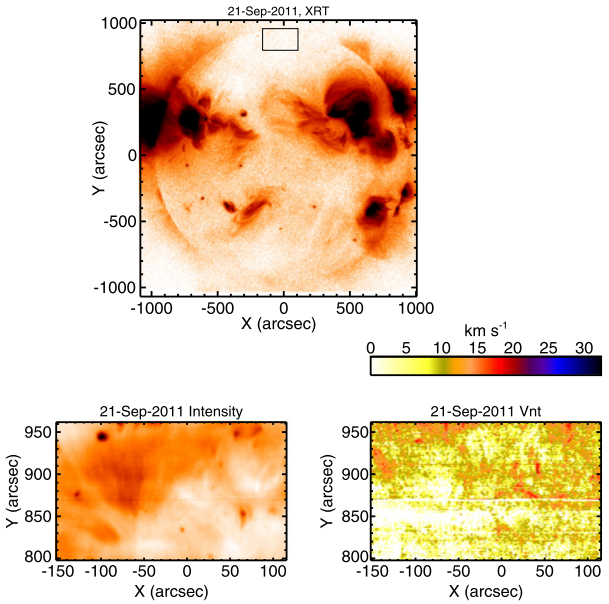

Figure 4 The top image shows the XRT image with the EIS field of view highlighted as a black box. The intensity plot (bottom left) and non-thermal velocity (bottom right) for 21 September 2011, later in Solar Cycle 23. Bright points are clearly evident in the intensity image, but there are no significant enhancements in $V_{\rm nt}$.

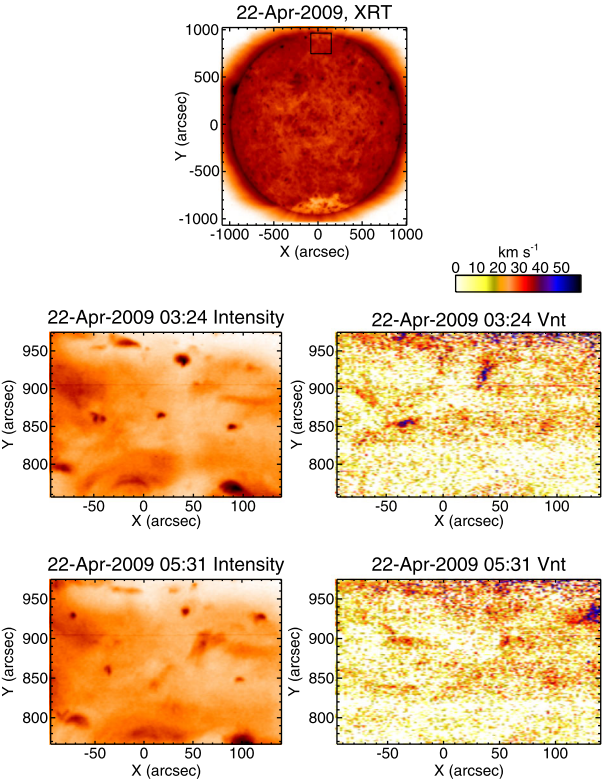

Figure 5 The top image shows the XRT image with the EIS field of view shown as a black box. The intensity plot (bottom left) and non-thermal velocity (bottom right) for two separate times on 22 April 2009. The upper raster starts at 03:24 UT, the lower one at 05:31 UT. Regions of enhanced non-thermal velocity are seen within the diffuse region at different locations. However, the non-thermal velocities are consistently higher in regions of weaker intensity.

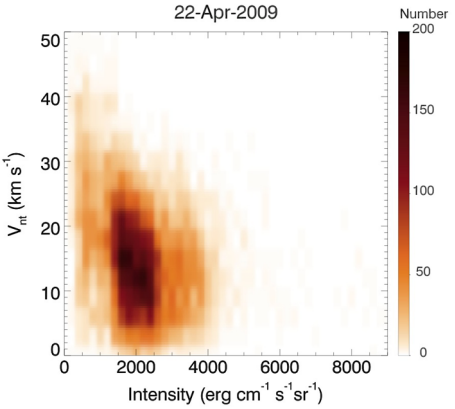

Figure 6 Non-thermal velocity vs intensity for the second raster shown in Figure 5. The colour indicates the number of pixels at each position. There is no strong relationship between intensity and non-thermal velocity, as can be seen in the images, but there is a trend for the lower V_{nt} values to be measured at higher intensities.

In Figure 8 a series of XRT images is shown, with the EIS field of view plotted as well. The series shows the different targets during a month – diffuse corona, coronal hole boundaries, and coronal holes are seen by EIS. This explains why a range of values can be observed in the same month when there are a number of rasters observed, as is seen in January 2012.

In Figure 9 the results of the histograms of V_{nt} for all the rasters in the south pole are plotted. The value of the peak of V_{nt} at the south pole is approximately constant from solar minimum to maximum, as was the case with the north pole. Although there is a long time lag between the polarity reversal at the north and south poles, there is no evidence of such a difference in the behaviour of V_{nt}. There is still evidence of the southern polar coronal hole as far on as mid-2012. Then it becomes dominated by diffuse corona, and the intensity increases beyond this point. Similarly to the north pole, there are more significant enhancements in V_{nt}^{upper} (defined from the histograms as 10 % of the peak of the histogram). The range of values drops as solar maximum approaches. It is well known that the polar coronal holes are largest at solar minimum. The trend for a reduced V_{nt}^{upper} may be due to the reduced coronal hole area with open magnetic field available, giving fewer opportunities for reconnection to occur between the open and closed magnetic field. In our data we did not distinguish between coronal hole and diffuse corona, and a range of targets is seen, as shown in Figure 8, but on a larger scale, these changes occur around our observing location. There is also a lag between the intensity in the north and south pole, as expected because of the lag of the polarity reversal at the two poles. The consistency between the behaviour of the north and south poles for V_{nt}^{peak} of the non-thermal velocity indicates that the general activity levels remain at similar levels throughout the cycle.

4. Comparing EIS V_{nt} Results with Global Magnetic PFSS Modelling

4.1. Tracking the Polarity Streams to the Poles

One of the ideas we wished to test was whether the unipolar magnetic streams create more small-scale activity at the polar regions when they reach high latitudes. To check this, we used the GONG magnetic butterfly diagram constructed for the period from late 2006 to late 2013 (see Figure 10). In 2010 there is a strong positive-polarity series of streams appearing towards the negative-polarity North polar regions, followed by another series starting in 2011. By 2013 the pole has changed polarity, the process having started in 2010. The streams

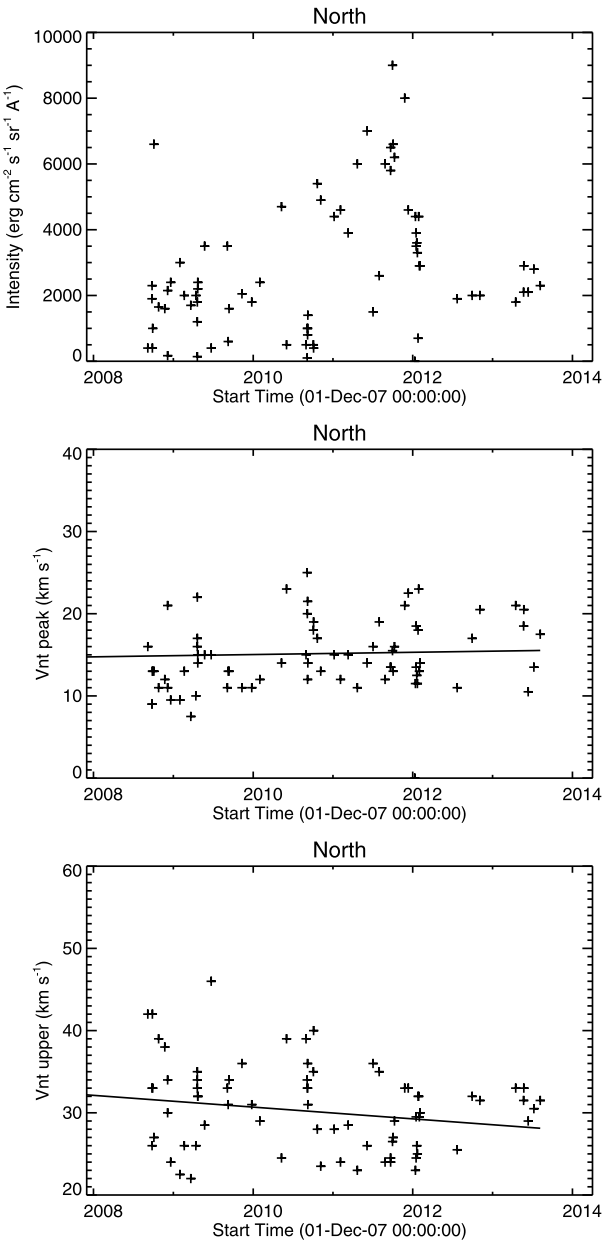

Figure 7 The data for the northern polar region observed by EIS from the end of 2007 to the end of 2013. The first plot shows the average intensity from EIS. The second plot shows the peak of the histogram of the non-thermal velocity. The third plot shows 10 % of the maximum of the non-thermal velocity histogram. A first-degree polynomial fit is shown as a straight line on the peak and $V_{\mathrm{nt}}^{\mathrm{upper}}$ plots.

moving towards the south pole behave differently. They begin with a positive-polarity stream (the same polarity as the south pole) in 2010, and the opposite polarity streams start in 2011. The polarity of the south pole has not completely changed by the end of this study period. The start of the intensity increases of both the north and south poles observed with EIS are consistent with the arrival of opposite-polarity streams at the poles.

If the polarity streams moving towards the poles would induce additional small-scale activity that would be measured by the non-thermal velocity, then changes should be seen at

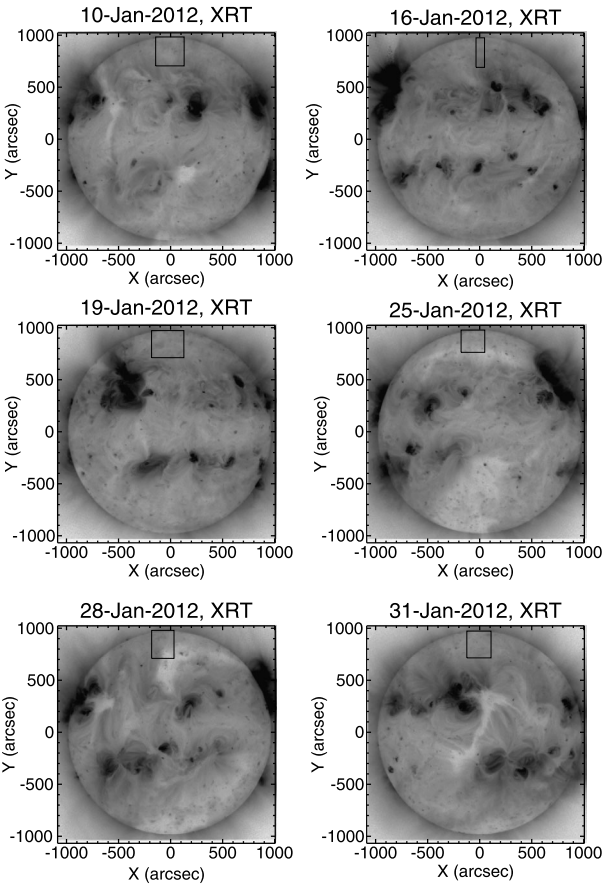

Figure 8 XRT images at different times during January 2012 with the EIS fields of view overlaid. The plot highlights the different locations and fields of view during a short time period.

the times when the streams reach the polar regions. However, there are no distinct differences at these times. In addition, we checked whether there was a change in the number of bright points at the poles. This was determined from SDO/AIA data (see Section 2). Figure 11 shows the number of coronal bright points and their change with the cycle. Figures 1 – 5 all show bright points, and these illustrate different stages of the solar cycle. As was shown with *Yohkoh* data, there is no change with solar cycle in the number of bright points. These small-scale features are a constant feature. This is consistent with the observations from the EIS data of $V_{\rm nt}^{\rm peak}$.

4.2. Comparing to the Number of Magnetic Nulls at High Latitudes

The number of magnetic nulls for this time period is illustrated in Figure 12. Section 2 describes the method. The number of nulls will indicate the regions with an increased likelihood for reconnection. The number of nulls can be seen to increase in the activity belt as the activity rises, as expected. As shown by Platten *et al.* (2014b), at solar minimum there are more nulls at lower latitudes and very few at high latitudes. This is because the polar fields are relatively strong at solar minimum, with a limited opposite-polarity field. As the streams of opposite polarity move to the poles, as seen in Figure 10, the number of nulls also increases at higher latitudes, as expected (*cf.* Figures 10 and 12).

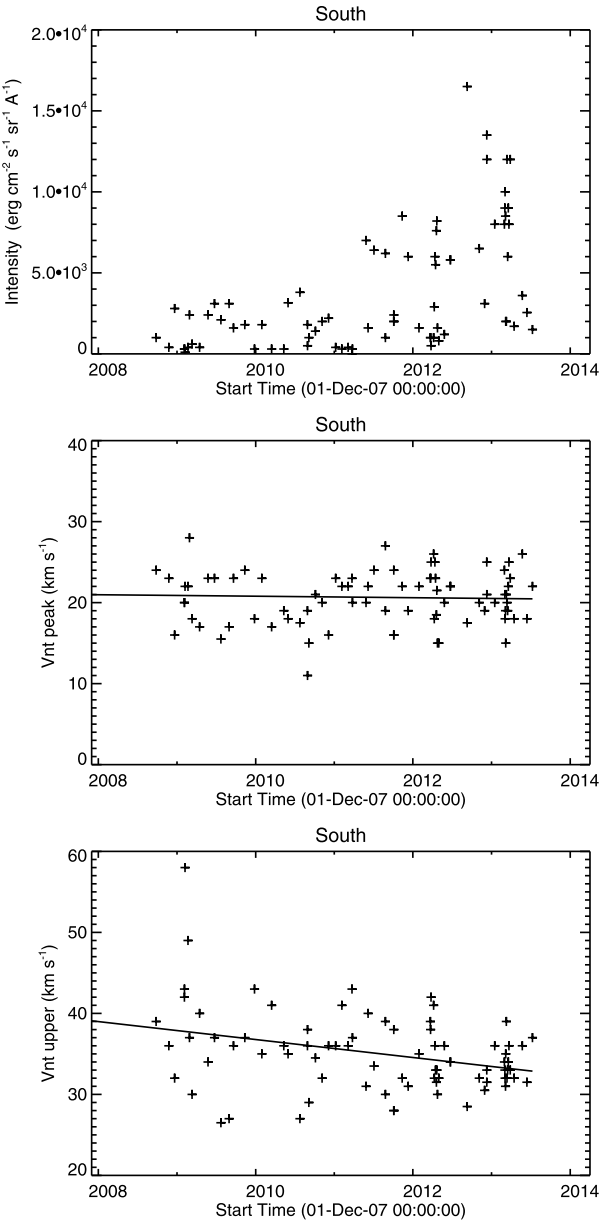

Figure 9 The data for the southern region observed by EIS from the end of 2007 to the end of 2013. The first plot shows the average intensity from EIS. The second plot shows the peak of the histogram of the non-thermal velocity. The third plot shows 10 % of the maximum of the non-thermal velocity histogram. A first-degree polynomial fit is shown as a straight line on the peak and $V_{\mathrm{nt}}^{\mathrm{upper}}$ plots.

Figure 13 shows the smoothed numbers of nulls for two separate height regions – showing those low in the atmosphere (below 1.1 $R_{\odot}$) and higher in the atmosphere (above 1.1 $R_{\odot}$), and all at higher than 50° latitude. Null points above 80° are not considered in Figure 13. The numbers of null points are smoothed using a running mean over 12 Carrington rotations to remove most of the noise in the data, and therefore the peaks will be real. At higher altitudes, there is much less variation. At lower altitudes there is variation, with the northern region showing a peak in 2010 that is consistent with the first strong opposite

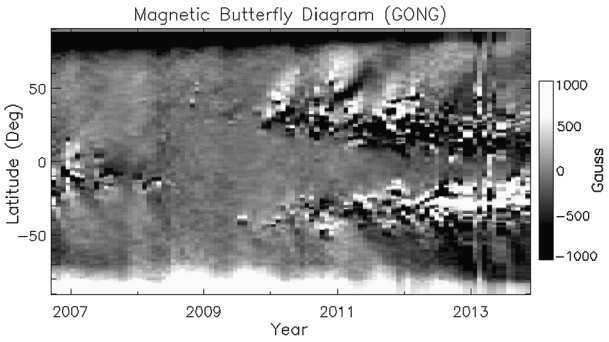

Figure 10 NSO/GONG butterfly diagram of net magnetic flux from 2007 – 2014. The poleward transport of magnetic flux from the active latitudes is evident from the black/negative and white/positive magnetic polarity streams.

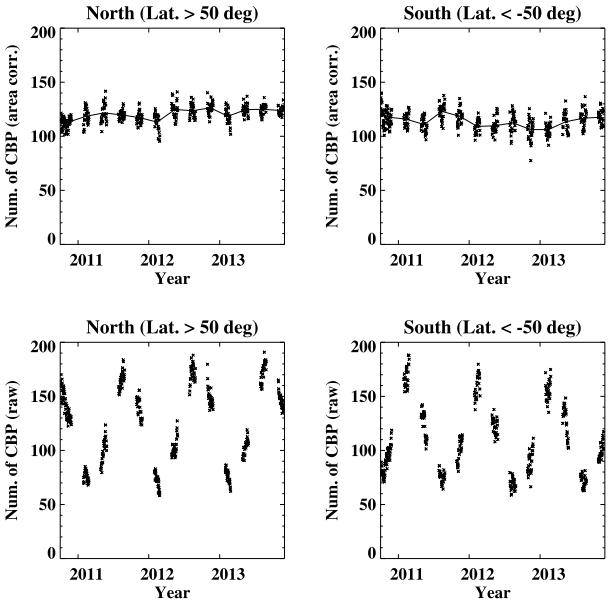

Figure 11 The number of coronal bright points determined from AIA 211 Å data from late 2010 to 2013. The top plots are adjusted for the seasonal variation in tilt. The solid lines are the monthly averages. The bottom figures are before the adjustment.

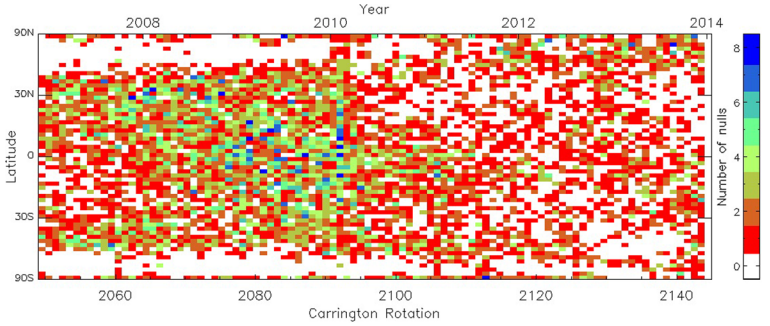

Figure 12 A butterfly diagram showing the number of nulls during the period of interest.

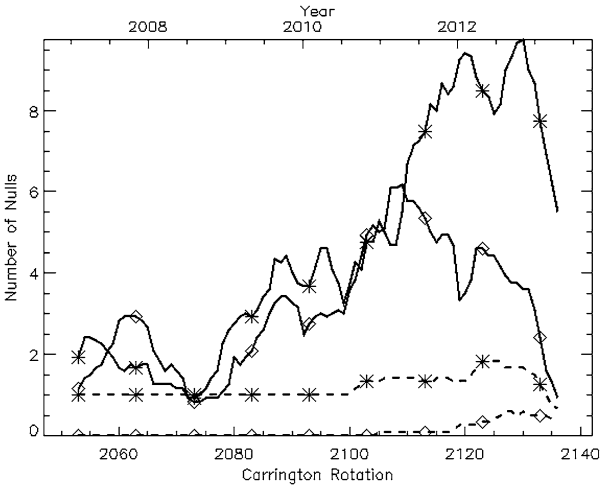

Figure 13 The smoothed number of nulls are shown. The black solid line with the stars shows the number of northern nulls below 1.1 $R_{\odot}$, the black dashed line with the stars shows the number of nulls in the North above 1.1 $R_{\odot}$. The black solid line with the diamonds shows the number of southern nulls below 1.1 $R_{\odot}$, and the black dashed line with the diamonds shows the number of southern nulls above 1.1 $R_{\odot}$. All of these plots show nulls above 50° latitude because we focus on the polar coronal hole surroundings.

polarity stream. There are fewer nulls followed by another rise beginning in 2011, which is consistent with the second opposite-polarity stream, which is extended and lasts until the start of 2013. In the South the nulls increase in 2010, have a peak in 2011, and then decrease steadily. A same-polarity stream arrives at the poles in 2010 to 2011, which could account for the change in the number of nulls. The opposite-polarity stream starts to arrive in 2012, but is very weak. It is interesting that the number of nulls in the South increases when a same-polarity stream arrives as well as when an opposite polarity stream arrives. This suggests that the poles have many mixed-polarity regions.

We can clearly see that there is a variation in the nulls below 1.1 $R_{\odot}$. However, no significant variation in the non-thermal velocity at the poles during the cycle is detected.

5. Discussion

We have analysed $V_{\rm nt}$ at the poles for a period of more than six years. The $V_{\rm nt}$ values provide insight into the dynamical behaviour of the poles that the intensity alone cannot do. We regularly observe enhanced $V_{\rm nt}$ features that do not have a high-intensity counterpart. The enhanced $V_{\rm nt}$ features are often bright points or are jet-shaped. The fact that these features are also seen in low-intensity regions suggests that the open magnetic regions are important in creating enhanced dynamical behaviour. This is to be expected from interchange reconnection with a closed and open magnetic field reconnecting. In addition, we observed enhanced $V_{\rm nt}$ values at the edge of the diffuse coronal regions. These are also regions where the larger-scale closed diffuse loops will interact with the open magnetic field. Madjarska *et al.* (2012) have shown how this interaction between an open and closed magnetic field at coronal hole boundaries is related to jets and bright points and induces the coronal hole boundary evolution that is observed.

We observe a change in intensity at the poles, with the north pole reaching a peak before the south pole. The north pole changes its polarity before the south pole, which means that these changes in intensity are expected. We globally modelled this to determine the number of nulls below 1.1 $R_{\odot}$ at the poles and to find significant changes over the cycle, as the magnetic polarity streams drift to the poles. The decaying active regions slowly diffuse to the poles with one polarity dominating. For the south pole, there initially is a magnetic

polarity stream with the same polarity as the south pole. As this stream reaches the pole, the existing nulls increase. This suggests that any change in the magnetic field will induce more nulls. We wished to test the hypothesis that these different polarity streams would induce increased dynamical activity at the poles. To do this, we studied $V_{\rm nt}$ over the same time period. We found that there is no significant change with the solar cycle. However, there is a reduction in the variation of the upper range of $V_{\rm nt}$ that highlights that strongly dynamical behaviour such as jets is reduced as the solar maximum approaches. This is probably because the reduced area of the polar coronal hole allows fewer opportunities for reconnection between open and closed magnetic fields. We also analysed the number of bright points at high latitudes and found that this value does not change with cycle either. We conclude that this dynamic activity is not related to large-scale changes that occur during the cycle. This has implications for the debate on whether there is a local as well as a global dynamo. It is well understood that the global dynamo is responsible for solar activity such as sunspots, flares, and coronal mass ejections. The cyclic behaviour is driven by the solar differential rotation. However, as described in the review by Stenflo (2013), the global dynamo creates magnetic fields at larger scales, which can cascade down the magnetic energy spectrum to much smaller scales. The distinguishing feature between local and global dynamo is that the local dynamo is decoupled from the activity cycle and forms the constant small-scale magnetic field pattern that exists on the Sun. Shiota *et al.* (2012) described the small magnetic bipoles that are observed throughout the cycle; the enhanced $V_{\rm nt}$ values are probably related to these small bipoles. The measurement of the number of bright points at high latitude corroborates this result.

These results also have implications for the formation of the fast solar wind. The continuous activity that is observed will create jets of plasma that will contribute to the fast solar wind. This contribution does not wane during solar minimum and remains a steady level during the cycle. In this work we are limited in exploring the polar regions because of line-of-sight effects. The future Solar Orbiter mission will be able to address this by getting out of the ecliptic and having a clearer view of the poles.

Acknowledgements We used data obtained by the *Global Oscillation Network Group* (GONG) Program, managed by the National Solar Observatory, which is operated by AURA, Inc. under a cooperative agreement with the National Science Foundation. The data were acquired by instruments operated by the Big Bear Solar Observatory, High Altitude Observatory, Learmonth Solar Observatory, Udaipur Solar Observatory, Instituto de Astrofísica de Canarias, and Cerro Tololo Interamerican Observatory. Data were used courtesy of NASA/SDO and the AIA and HMI science teams. *Hinode* is a Japanese mission developed and launched by ISAS/JAXA, collaborating with NAOJ as a domestic partner, NASA and STFC (UK) as international partners. Scientific operation of the *Hinode* mission is conducted by the *Hinode* science team organised at ISAS/JAXA. This team mainly consists of scientists from institutes in the partner countries. Support for the post-launch operation is provided by JAXA and NAOJ (Japan), STFC (UK), NASA, ESA, and NSC (Norway). We acknowledge the Leverhulme Trust for funding the 'Probing the Sun: inside and out' project upon which this research is based. LvDG acknowledges the Hungarian government for grants OTKA K-081421 and K-109276. DB thanks STFC for support under Consolidated Grant ST/H00260/1. This project has received funding from the European Union's Seventh Programme for Research, Technological Development and Demonstration under Grant Agreement No. 284461 – Project eHeroes (www.eheroes.eu).

References

Altschuler, M.D., Newkirk, G.: 1969, Magnetic fields and the structure of the solar corona. I: Methods of calculating coronal fields. *Solar Phys.* **9**, 131. DOI. ADS.

Babcock, H.D.: 1959, The Sun's polar magnetic field. *Astrophys. J.* **130**, 364. DOI. ADS.

Culhane, J.L., Harra, L.K., James, A.M., Al-Janabi, K., Bradley, L.J., Chaudry, R.A., Rees, K., Tandy, J.A., Thomas, P., Whillock, M.C.R., Winter, B., Doschek, G.A., Korendyke, C.M., Brown, C.M., Myers, S.,

Mariska, J., Seely, J., Lang, J., Kent, B.J., Shaughnessy, B.M., Young, P.R., Simnett, G.M., Castelli, C.M., Mahmoud, S., Mapson-Menard, H., Probyn, B.J., Thomas, R.J., Davila, J., Dere, K., Windt, D., Shea, J., Hagood, R., Moye, R., Hara, H., Watanabe, T., Matsuzaki, K., Kosugi, T., Hansteen, V., Wikstol, Ø.: 2007, The EUV Imaging Spectrometer for Hinode. *Solar Phys.* **243**, 19. DOI. ADS.

Davis, J.M.: 1983, X-ray bright points and the sunspot cycle – further results and predictions. *Solar Phys.* **88**, 337. DOI. ADS.

Delaboudinière, J.-P., Artzner, G.E., Brunaud, J., Gabriel, A.H., Hochedez, J.F., Millier, F., Song, X.Y., Au, B., Dere, K.P., Howard, R.A., Kreplin, R., Michels, D.J., Moses, J.D., Defise, J.M., Jamar, C., Rochus, P., Chauvineau, J.P., Marioge, J.P., Catura, R.C., Lemen, J.R., Shing, L., Stern, R.A., Gurman, J.B., Neupert, W.M., Maucherat, A., Clette, F., Cugnon, P., van Dessel, E.L.: 1995, EIT: Extreme-Ultraviolet Imaging Telescope for the SOHO mission. *Solar Phys.* **162**, 291. DOI. ADS.

Doschek, G.A., Landi, E., Warren, H.P., Harra, L.K.: 2010, Bright points and jets in polar coronal holes observed by the Extreme-Ultraviolet Imaging Spectrometer on Hinode. *Astrophys. J.* **710**, 1806. DOI. ADS.

Freeland, S.L., Handy, B.N.: 1998, Data analysis with the SolarSoft system. *Solar Phys.* **182**, 497. DOI. ADS.

Golub, L., Krieger, A.S., Silk, J.K., Timothy, A.F., Vaiana, G.S.: 1974, Solar X-ray bright points. *Astrophys. J. Lett.* **189**, L93. DOI. ADS.

Golub, L., Deluca, E., Austin, G., Bookbinder, J., Caldwell, D., Cheimets, P., Cirtain, J., Cosmo, M., Reid, P., Sette, A., Weber, M., Sakao, T., Kano, R., Shibasaki, K., Hara, H., Tsuneta, S., Kumagai, K., Tamura, T., Shimojo, M., McCracken, J., Carpenter, J., Haight, H., Siler, R., Wright, E., Tucker, J., Rutledge, H., Barbera, M., Peres, G., Varisco, S.: 2007, The X-Ray Telescope (XRT) for the Hinode mission. *Solar Phys.* **243**, 63. DOI. ADS.

Gosain, S., Pevtsov, A.A., Rudenko, G.V., Anfinogentov, S.A.: 2013, First synoptic maps of photospheric vector magnetic field from SOLIS/VSM: Non-radial magnetic fields and hemispheric pattern of helicity. *Astrophys. J.* **772**, 52. DOI. ADS.

Hara, H., Nakakubo-Morimoto, K.: 2003, Variation of the X-ray bright point number over the solar activity cycle. *Astrophys. J.* **589**, 1062. DOI. ADS.

Hathaway, D.H.: 2010, The solar cycle. *Living Rev. Solar Phys.* **7**(1). DOI. ADS. http://solarphysics.livingreviews.org/Articles/lrsp-2010-1/.

Haynes, A.L., Parnell, C.E.: 2007, A trilinear method for finding null points in a three-dimensional vector space. *Phys. Plasmas* **14**, 082107. DOI. ADS.

Howe, R., Christensen-Dalsgaard, J., Hill, F., Komm, R., Larson, T.P., Rempel, M., Schou, J., Thompson, M.J.: 2013, The high-latitude branch of the solar torsional oscillation in the rising phase of Cycle 24. *Astrophys. J. Lett.* **767**, L20. DOI. ADS.

Kamio, S., Hara, H., Watanabe, T., Curdt, W.: 2009, Distribution of jets and magnetic fields in a coronal hole. *Astron. Astrophys.* **502**, 345. DOI. ADS.

Lemen, J.R., Title, A.M., Akin, D.J., Boerner, P.F., Chou, C., Drake, J.F., Duncan, D.W., Edwards, C.G., Friedlaender, F.M., Heyman, G.F., Hurlburt, N.E., Katz, N.L., Kushner, G.D., Levay, M., Lindgren, R.W., Mathur, D.P., McFeaters, E.L., Mitchell, S., Rehse, R.A., Schrijver, C.J., Springer, L.A., Stern, R.A., Tarbell, T.D., Wuelser, J.-P., Wolfson, C.J., Yanari, C., Bookbinder, J.A., Cheimets, P.N., Caldwell, D., Deluca, E.E., Gates, R., Golub, L., Park, S., Podgorski, W.A., Bush, R.I., Scherrer, P.H., Gummin, M.A., Smith, P., Auker, G., Jerram, P., Pool, P., Soufli, R., Windt, D.L., Beardsley, S., Clapp, M., Lang, J., Waltham, N.: 2012, The Atmospheric Imaging Assembly (AIA) on the Solar Dynamics Observatory (SDO). *Solar Phys.* **275**, 17. DOI. ADS.

Madjarska, M.S., Huang, Z., Doyle, J.G., Subramanian, S.: 2012, Coronal hole boundaries evolution at small scales. III. EIS and SUMER views. *Astron. Astrophys.* **545**, A67. DOI. ADS.

Mariska, J.T.: 1994, Flare plasma dynamics observed with the YOHKOH Bragg Crystal Spectrometer. 2: Properties of the Fe XXV, CA XIX. *Astrophys. J.* **434**, 756. DOI. ADS.

McIntosh, S.W., Gurman, J.B.: 2005, Nine years of EUV bright points. *Solar Phys.* **228**, 285. DOI. ADS.

Mordvinov, A.V., Yazev, S.A.: 2014, Reversals of the Sun's polar magnetic fields in relation to activity complexes and coronal holes. *Solar Phys.* **289**, 1971. DOI. ADS.

Morgan, H., Habbal, S.R.: 2010, Observational aspects of the three-dimensional coronal structure over a solar activity cycle. *Astrophys. J.* **710**, 1. DOI. ADS.

Ogawara, Y., Takano, T., Kato, T., Kosugi, T., Tsuneta, S., Watanabe, T., Kondo, I., Uchida, Y.: 1991, The SOLAR-A mission – an overview. *Solar Phys.* **136**, 1. DOI. ADS.

Petrie, G.J.D., Petrovay, K., Schatten, K.: 2014, Solar polar fields and the 22-year activity cycle: observations and models. *Space Sci. Rev.*. DOI. ADS.

Pinto, R.F., Brun, A.S., Jouve, L., Grappin, R.: 2011, Coupling the solar dynamo and the corona: wind properties, mass, and momentum losses during an activity cycle. *Astrophys. J.* **737**, 72. DOI. ADS.

Platten, S.J., Parnell, C.E., Haynes, A.L., Priest, E.R., Mackay, D.H.: 2014a, The solar cycle variation of topological structures in the global solar corona. *Astron. Astrophys.* **565**, A44. DOI. ADS.

Platten, S.J., Parnell, C.E., Haynes, A.L., Priest, E.R., Mackay, D.H.: 2014b, The solar cycle variation of topological structures in the global solar corona. *Astron. Astrophys.* **565**, A44. DOI. ADS.

Sattarov, I., Pevtsov, A.A., Karachik, N.V., Sherdanov, C.T., Tillaboev, A.M.: 2010, Solar Cycle 23 in coronal bright points. *Solar Phys.* **262**, 321. DOI. ADS.

Schatten, K.H., Wilcox, J.M., Ness, N.F.: 1969, A model of interplanetary and coronal magnetic fields. *Solar Phys.* **6**, 442. DOI. ADS.

Seaton, D.B., De Groof, A., Shearer, P., Berghmans, D., Nicula, B.: 2013, SWAP observations of the long-term, large-scale evolution of the extreme-ultraviolet solar corona. *Astrophys. J.* **777**, 72. DOI. ADS.

Shiota, D., Tsuneta, S., Shimojo, M., Sako, N., Orozco Suárez, D., Ishikawa, R.: 2012, Polar field reversal observations with Hinode. *Astrophys. J.* **753**, 157. DOI. ADS.

Stenflo, J.O.: 2013, Solar magnetic fields as revealed by Stokes polarimetry. *Astron. Astrophys. Rev.* **21**, 66. DOI. ADS.

Tsuneta, S., Ichimoto, K., Katsukawa, Y., Lites, B.W., Matsuzaki, K., Nagata, S., Orozco Suárez, D., Shimizu, T., Shimojo, M., Shine, R.A., Suematsu, Y., Suzuki, T.K., Tarbell, T.D., Title, A.M.: 2008, The magnetic landscape of the Sun's polar region. *Astrophys. J.* **688**, 1374. DOI. ADS.

Yeates, A.R.: 2014, Coronal magnetic field evolution from 1996 to 2012: Continuous non-potential simulations. *Solar Phys.* **289**, 631. DOI. ADS.